Atomistic simulations of ettringite and its aqueous interfaces: Structure and properties revisited with the modified ClayFF force field

Evgeny V. Tararushkin, Vasily V. Pisarev, Andrey G. Kalinichev

Version of Record: https://www.sciencedirect.com/science/article/pii/S0008884622000503
Manuscript_66b9dd5c615a6507f6cc0e2769026d55

Atomistic simulations of ettringite and its aqueous interfaces: Structure and properties revisited with the modified ClayFF force field

Evgeny V. Tararushkin[1,2], Vasily V. Pisarev[1,3], Andrey G. Kalinichev[1,4,*]

[1] National Research University Higher School of Economics, Moscow, Russian Federation

[2] Russian University of Transport, Moscow, Russian Federation

[3] Joint Institute for High Temperatures of the Russian Academy of Sciences, Moscow, Russia

[4] Laboratoire SUBATECH (UMR 6457 – IMT-Atlantique, Université de Nantes, CNRS/IN2P3), Nantes, France

*Corresponding author: Andrey G. Kalinichev (kalinich@subatech.in2p3.fr)

Keywords: ettringite, molecular modeling, crystal structure, elastic properties, adsorption, diffusion, hydrogen bonding

ABSTRACT

Ettringite, ($Ca_6[Al(OH)_6]_2[SO_4]_3 \cdot nH_2O$, n = 24-27), is one of the common phases of cement and plays an important role in cement chemistry as the primary cause of sulphate corrosion in Portland cement. Molecular dynamic computer simulations have already been applied earlier to model the crystal structure of ettringite and its interfaces with aqueous salt solutions. A recently developed version of the widely used ClayFF force field allows now to explicitly take into account the bending of M-O-H angles of (M=Al, Ca), leading to a much better agreement of the simulation results with available experimental data. The structure and dynamics of bulk ettringite crystal and its interfaces with NaCl and Na_2SO_4 aqueous solutions are quantitatively evaluated here for the new modified version of the force field, ClayFF-MOH, and compared with the results obtained with the earlier version, ClayFF-orig. The crystallographic parameters, elastic properties, the structure and dynamics of intracrystalline hydrogen bonding network and the vibrational spectra of ettringite are calculated by classical molecular dynamics simulations and quantitatively compared with available experimental data using both versions of ClayFF. Atomic density profiles for solution species at the ettringite surface, atomic distributions within the crystal-solution interface, and the interfacial diffusional mobility of the species are also calculated and compared. The results clearly demonstrate the importance of the explicit inclusion of M-O-H angular bending terms for accurate modeling of the mineral systems containing structural and interfacial hydroxide groups. The simulation results also show that the application of the new more accurate ClayFF-MOH version of the force field leads to the formation of a stronger hydrogen bonding network structure in the intercolumnar space of the ettringite crystal and at its surface, resulting in a stronger immobilization of the water molecules involved, as well as the ions. The ionic adsorption at the ettringite surface is also generally stronger than it was predicted by the earlier model.

1. INTRODUCTION

Portland cement is the most common man-made construction material. It is composed of a large number of hydration phases, and detailed understanding of their properties and behavior is crucial for optimizing the manufacturing process and predicting its long-term durability [1-3].

Ettringite is one of the common phases appearing during the hydration of Portland cement [4, 5] and during its operation after hardening, for example, during an external sulphate attack [6]. In cement systems, ettringite plays both positive and negative roles. Early ettringite formation (EEF) during the onset of Portland cement hydration can positively affect the initial strength development of the hardening cement mortar [7]. At the same time, the negative role of ettringite is much more important than its positive role. Ettringite is a product of the sulfate attack on cements and concretes. The interaction of concrete with sulphate waters can lead to the penetration of sulphate ions into the pores of the cement mortar, where a new ettringite phase can form and the amount of the previously formed ettringite can increase [9]. This additional ettringite formation leads to its volume expansion and cracking resulting in mechanical damage of concrete. Similar damage can also result from the manufacturing of concrete structures at elevated temperatures of 65-70°C. In this case, delayed ettringite formation occurs [9], which causes mechanical damage of concrete even without an external sulphate attack on the cement paste.

Ettringite is calcium trihydrosulphoaluminate ($Ca_6[Al(OH)_6]_2[SO_4]_3 \cdot nH_2O$, n = 24-27), which belongs to the AFt-phase of cement [10]. As a natural mineral, ettringite was first discovered by Lehmann in 1874 [11]. In today's nomenclature, the ettringite crystallographic group also includes thaumasite, benthorite, and other aqueous sulphates of Ca and Al [12].

The primary starting components for the formation of ettringite in cement are the products of the

C-S-H phase [Ca^{2+}, OH^-, H_2O], the products of monosulphates [Ca^{2+}, SO_4^{2-}, OH^-, $Al(OH)_4^-$, H_2O], and dissolved ions from the aqueous phase $(SO_4)^{2-}$ in the pores of the forming cement mortar [9,10]. From these components ettringite is formed by the following reaction [9]:

$$6Ca^{2+}+2Al(OH)_4^-+4OH^-+3SO_4^{2-}+26H_2O \rightarrow Ca_6[Al(OH)_6]_2[SO_4]_3\cdot 26H_2O \quad (1)$$

Due to the above mentioned effects of ettringite formation and evolution for the concrete mechanical stability and durability, it is very important to have a detailed understanding of these processes on the fundamental molecular scale. Along with various different methods of molecular-scale experimental characterization of cementitious materials, atomistic computer simulations are rapidly emerging as a very powerful and informative tool [1, 13-16]. Various methods of atomistic modeling — classical molecular dynamics (MD) and Monte Carlo (MC) simulations, quantum density functional theoretical methods (DFT), etc. — are increasingly used to simulate the structure and properties of cementitious materials [17-19]: non-hydrated phases of Portland cement [20], hydrated phases (C-S-H, portlandite, etc.) [21], as well as to model their interaction with water and aqueous solutions of different ionic compositions [22-34]. In particular, interaction of aqueous solutions with ettringite surfaces has also been a subject of several atomistic computer simulation studies [21, 22, 35].

Over the last 10-15 years, numerous force field models for classical atomistic simulations have been developed and successfully applied for cementitious materials [21, 36-38]. Their relative advantages and disadvantages have been recently comprehensively reviewed [16].

ClayFF [39] is one of the popular and widely used force fields already thoroughly tested in the atomistic simulations of a wide range of clay- and cement-related materials [16, 40-42]. It is based on a simplifying assumption that the majority of interatomic interactions in the crystals are quasi-ionic and can be relatively accurately described by a combination of electrostatic and van-der-Waals forces [39]. In addition to electrostatic (Coulomb) and short-range non-bonded (vdW) interactions, ClayFF also contains a small number of explicit bonded interactions (e.g., bond stretch, angle bend). This force field has already been applied multiple times for the atomistic simulations of ettringite and its interfaces with aqueous solutions [21, 32, 35]. Recently, the parametrization of ClayFF has been specifically modified to reproduce elastic properties of ettringite and monosulfoaluminate [43]. Here we are using another new modification of ClayFF, that has been developed to allow a significantly more accurate modeling of the surfaces and edges of clay particles by introducing explicit Metal−O−H angle bending terms [40, 44, 45]. Ettringite contains similar terms for aluminum and calcium (Al−O−H and Ca−O−H), and we apply this new modification in classical MD simulations to quantify its effects on the predicted structure and properties of bulk ettringite cyrstals and their aqueous interfaces with $NaCl/Na_2SO_4$ solutions.

2. MODELS AND METHODS

2.1. Structural Models

The crystal structure of ettringite is formed by the columns of stacked aluminum and calcium hydroxide polyhedra oriented along the *c* crystallographic axis. Aluminum ions located along the central axes of the columns are sixfold coordinated with hydroxyls. Calcium ions are located at the periphery of the columns, and their highly distorted coordination polyhedron is formed by the same structural hydroxyls, but also by the intercolumnar H_2O

molecules. Simultaneously, these water molecules contribute to the hydration shells of intercolumnar sulphate ions.

Ettringite crystal structure has the *P*31*c* symmetry with lattice parameters $a = b =$ 11.17÷11.26 Å and c = 21.35÷21.48 Å [46-49]. The ettringite density is measured to be 1.76÷1.90 $g \cdot cm^{-3}$ [47-49] and the experimentally determined number of H_2O molecules in the unit cell varies between 24 and 27, with 26 being the most common number [47-49]. At the same time, the DFT calculations [24] show only a very weak dependence of the unit cell parameters on the amount of H_2O molecules present: the *a* and *b* parameters increase by about 1% per each additional H_2O molecule, while *c* increases by only 0.25%. Therefore, for our models, we have adopted n_{H2O} = 26 and the crystallographic parameters of ettringite, $Ca_6[Al(OH)_6]_2[SO_4]_3 \cdot 26H_2O$, as reported by Moore and Taylor [47].

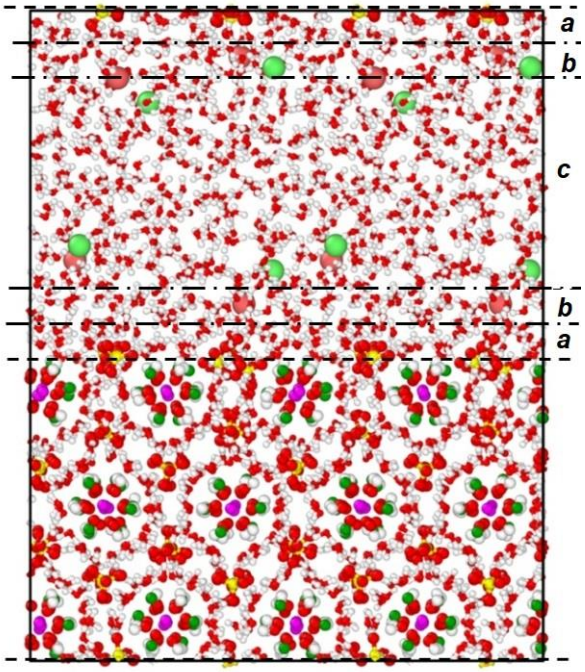

Figure 1. A representative snapshot of the simulation supercell of ettringite with NaCl aqueous solution. Violet atoms – Al, dark green atoms – Ca, red atoms – O, white atoms – H, yellow atoms – S, pale pink atoms – Na, light green atoms – Cl.

Dashed lines indicate the conditional position of the crystal-solution interfaces on both sides of the ettringite crystal. Dashed-dotted lines schematically indicate the first 3.5Å (*a*) and second 3.5Å (*b*) layers of solution next to the surface. Beyond the layer (*b*) we consider the solution to be in nearly the bulk phase (*c*).

The simulation supercell of ettringite contained 4×2×2 crystallographic unit cells in the *a*, *b*, and *c* directions, respectively. To simulate the aqueous interfaces of this crystal, the optimized model supercell was cleaved parallel to the (1 0 0) plane, which is the natural perfect cleavage face of ettringite crystals [49, 50] and is commonly used in the simulations of ettringite-solution interfaces (e.g., [21, 35]). The created surfaces were brought into contact with a layer of NaCl or Na_2SO_4 aqueous solution, that was approximately 30 Å thick, to provide for a more accurate comparison with the earlier simulated models [21]. The number of H_2O molecules in the aqueous nanopore was selected to reproduce the density of the aqueous solution under ambient conditions (~1 g/cm^3). The Na^+, Cl^- and SO_4^{2-} ions were initially uniformly distributed in the nanopore. The nominal NaCl solution concentration in the pore space was ~0.5M (1568 H_2O molecules and 32 ions), while it was ~0.4M (1568 H_2O molecules and 24 ions) in the case of Na_2SO_4. Compared to the experimentally studied values (e.g., [9, 22]), these concentrations are relatively high, but are commonly used in the molecular simulations of interfacial solutions for better statistical sampling [13, 21, 30, 31].

Periodic boundary conditions were applied in all three dimensions to produce models of the interfaces formed by the crystal ettringite layers interspersed with layers of aqueous solutions. The thickness of the solution layer was sufficiently large to effectively exclude direct interactions between two different solution/solid interfaces created because of the periodicity of the system [21]. As a result, the dimensions of the simulation supercell for ettringite with aqueous NaCl or Na_2SO_4 solution were 43×44×56 Å^3 (Fig. 1).

2.2 Force Field Parameters

The MD simulations were performed with the new modified version of the force field (ClayFF-MOH) [44] and with the original parametrization (ClayFF-orig) [39] for comparison. ClayFF assigns partial charges of different structural oxygen atoms by taking into account, when necessary, their local coordination to the tetrahedral and/or octahedral substituting atoms in the crystal structure [39, 42]. The values of the additional parameters for Metal–O–H (M–O–H) angle bending terms of the more recent ClayFF-MOH version were determined for Mg–O–H, Al–O–H [44], and Si–O–H [45] angles by fitting the results of classical MD simulations to the structural and dynamic results of DFT calculations of brucite, $Mg(OH)_2$, gibbsite, $Al(OH)_3$, and kaolinite, $Al_2Si_2O_5(OH)_4$, respectively, using the simple harmonic functional form:

$$E_{\text{MOH-bend}} = k\,(\theta - \theta_0)^2, \tag{1}$$

where θ is the angle ∠M–O–H, θ_0 is its equilibrium value, and k is the bending force constant.

The optimized parameters for Al–O–H and Mg–O–H angles are as follows: $\theta_{0,\text{AlOH}} = \theta_{0,\text{MgOH}} = 110^{\text{o}}$, $k_{\text{AlOH}} = 15$ kcal·mol^{-1}·rad^{-2}, and $k_{\text{MgOH}} = 6$ kcal·mol^{-1}·rad^{-2}. In the ettringite structure, the Al–O–H bending term controls the orientation of O–H groups of the aluminum $[Al(OH)_6]^{3-}$ octahedron, while the Ca–O–H bending term controls the orientation of the four O–H groups coordinating the Ca-polyhedron [49]. The H_2O molecules completing the coordination of calcium are not bound by this term and are free to move in the intercolumnar space of the crystal or on its surface. In this work, the parameters for the Al–O–H bending term were assumed to be the same as those of gibbsite, while the parameters for the Ca–O–H bending were assumed to be identical to those of Mg–O–H, based on the close similarity between the $Mg(OH)_2$ and $Ca(OH)_2$ crystal structures.

2.3 Simulation Details

LAMMPS software package [51] was used to perform the MD simulations. The atomic equations of motion were numerically integrated with a time step of 1.0 fs. The constructed atomistic models were initially equilibrated for 1 ns by *NVT*-ensemble simulation at the ambient temperature of 298 K using the Nosé-Hoover thermostat [52]. After the *NVT* equilibration, the equilibrium *NVE*-simulation was performed to collect the dynamic trajectories of atoms for further statistical analysis. The *NVE* part was also 1.0 ns long, and the trajectories are recorded every 100 time steps to ensure good statistical accuracy of the subsequent data analysis. To calculate unit cell parameters and density of bulk ettringite crystals, a separate equilibrium *NPT*-ensemble simulation run was also performed at 298 K and 1 bar using the using the Nosé-Hoover barostat [52].

2.4. Simulations of Bulk Crystal Properties

In addition to the crystallographic parameters, for the bulk ettrigite phase we also evaluated the elastic constants, vibrational spectra, and the dynamics of the hydrogen bonds formed and transformed between different H_2O molecules,–OH groups, and SO_4^{2-} ions in the crystal structure.

The elastic constants of ettringite under normal conditions were calculated in a series of special equilibrium MD runs. First, the stress tensor components as the sum of the kinetic and virial terms were calculated for the equilibrium intact supercell, which was obtained after *NPT*-simulations. Then, the negative and positive supercell deformations of 1.0% were specified for six independent directions, and the stress tensor components were calculated for the specified deformations. The calculations for intact and deformed ettringite supercells were carried out in *NVT* ensemble for 0.5 ns. The elastic constants the crystal were numerically determined according to the generalized Hooke's law:

$$C_{ijkl} = \frac{\partial \sigma_{ij}}{\partial \varepsilon_{kl}}\Big|_{T,\varepsilon_{kl}}, \quad (2)$$

where σ_{ij} – stress tensor components, ε_{kl} – strain tensor components. The bulk modulus (*K*), shear modulus (*G*), Young modulus (*E*), and Poisson ratio (*v*), of ettringite were also obtained using the Voigt-Reuss-Hill (VRH) approximation, following the work of Honorio et al. [43].

The power spectrum (PS), or the classical density of vibrational states (DOS), provides useful information about the dynamics of vibrational modes characterizing the atomic thermal motions in ettringite. The PS was obtained as Fourier transformations of the velocity autocorrelation functions (VACF) (e.g., [52]:

$$\mathrm{PS}(\omega) = \sum_{t=1}^{n_{\mathrm{VACF}}} \mathrm{VACF}(t) \cdot \cos\left(\frac{\pi}{n_{\mathrm{VACF}}} \cdot t \cdot \omega\right), \quad (3)$$

where n_{VACF} is the number of MD trajectory "windows" used in a particular calculation of VACF. The normalized VACFs were calculated from the MD-simulated dynamic trajectories for the entire system, as well as for selected subsets of atoms in it [52]:

$$\mathrm{VACF}(t) = \sum_{f=1}^{n-n_{\mathrm{VACF}}} \sum_{\mathrm{sel.atoms}} \vec{v}_f \cdot \vec{v}_{f+t} \Big/ \sum_{f=1}^{n-n_{\mathrm{VACF}}} \sum_{\mathrm{sel.atoms}} \vec{v}_f \cdot \vec{v}_f , \quad (4)$$

where *n* is the total number of "windows"; v_{f} and $v_{\mathrm{f+t}}$ are velocities at windows *f* and *f*+*t*, respectively. To reduce the statistical noise, especially for the fastest moving hydrogen atoms, a filtering function was the applied (e.g., [53]):

$$\mathrm{VACF}(t) = \mathrm{VACF}(t) \cdot exp(-t/\tau) , \quad (5)$$

where τ was set to 0.25 ps.

The VACF and PS were calculated for all atoms of ettringite and separately for each atom of ettringite. We also calculated components of the VACF tensors along individual

crystallographic directions to investigate the vibrational modes parallel to the ettringite columns (*zz*) and perpendicular to them (*xy*).

The structure and dynamics of the intra-crystalline hydrogen bond network plays a major role in keeping the crystal together and defining its properties (e.g., [24]). The properties of this network are expected to be particularly affected by the introduction of the additional M–O–H angle bending term in the ClayFF force field [45]. Therefore, the behavior of the intra-crystalline network of H-bonds in ettringite was carefully analyzed for both versions of ClayFF, taking into account all possible pairs of donors and acceptors of H-bonds in the crystal. The hydrogen atoms of H_2O molecules and structural –O–H groups are considered here as donors, while the oxygen atoms of H_2O molecules, SO_4^{2-} ions, and structural –O–H groups are considered as acceptors of H-bonds in the crystal structure.

To define an H-bond between a donor and acceptor, a common geometrical definition was used, according to which an H-bond exists if the donor-acceptor distance is less than 2.45 Å, and the angle between the H-bond direction and the vector connecting the donor and acceptor oxygen atoms is less than 30° (e.g., [54, 55]).

To estimate the lifetime of hydrogen bonds for the pairs under consideration, continuous time correlation functions of H-bonds were calculated [56, 57]:

$$S(t) = \frac{\langle h(0) \cdot H(t) \rangle}{\langle h \rangle}, \quad (6)$$

where $h(t)$ and $H(t)$– hydrogen bond population variables [56]. The variable $h(t)$ is unity when a particular donor-acceptor pair is H-bonded at time *t* according to the definition above, and zero otherwise. The variable $H(t)$, on the other hand, is defined as unity, when the tagged pair of sites remain continuously hydrogen bonded from time $t = 0$ to time t, and zero otherwise [56, 57]. The H-bonding time correlation functions for every possible donor-acceptor pair were calculated from the equilibrium MD trajectories with a time "window" of

10 ps and an offset of 10 fs. The average lifetimes τ for various types of H-bonds were then assessed by integrating the time correlation functions $S(t)$ [56]:

$$\langle \tau \rangle = \int_0^\infty S(t)dt \,, \tag{7}$$

where averaging is taken over all H-bonds of the same type that ever existed along the equilibrium MD trajectory analyzed.

2.5. Simulations of Ettringite-Solution Interfaces

Structural and dynamic properties of the simulated ettringite-solution interfaces were obtained from the statistical analysis of the equilibrium *NVE*-simulations. Atomic density profiles, $\rho_\alpha(z)$, for aqueous species as functions of their distance from the crystal surface, were determined as the average number of atoms of a certain type α in a slice of thickness Δz parallel to the ettringite surface, normalized by the system volume, V (e.g., [42]):

$$\rho_\alpha(\Delta z) = \frac{\langle N_\alpha(\Delta z)\rangle}{V} \,. \tag{8}$$

The position of the interface was symbolically defined as the time-averaged position of the oxygen atoms of the crystal that are nearest to the solution (e.g., [21, 55]) (see Fig.1).

$$\rho_\alpha(x,y) = \frac{\langle N_\alpha(\Delta x \Delta y)\rangle}{\Delta x \Delta y}. \tag{9}$$

The self-diffusion coefficients D of interlayer species were determined from their mean squared displacement (MSD) according to the Einstein relationship [52]:

$$D = \lim_{t\to\infty} \sum_{i=1}^{N} \langle |r_i(t) - r_i(t_o)|^2 \rangle \Big/ 2dNt \,, \tag{10}$$

where N is the total number of diffusing species and d is the dimensionality of the system. Here we used $d = 3$ for calculations of the "bulk" diffusion coefficients of species in the entire ~30Å-thick aqueous solution layer between the surfaces of ettringite. In addition, following the common definition of quasi-two-dimensional diffusional mobility of aqueous species at a solid surface (e.g., [42]), we estimated such diffusion coefficients ($d = 2$) within the first and second 3.5 Å slices of the solution next to the ettringite surface, as defined above. However, it has to be noted that due to the relatively small system size of the simulated models and the periodic boundary conditions used, the diffusion coefficients presented here can only be considered as semi-quantitative and are used here primarily for comparisons between different force field models and different solution composition within the same model setting.

3. RESULTS AND DISCUSSION

3.1. Crystallographic parameters

Table 1. Crystallographic unit cell parameters and density of ettringite: Simulated results and experimental data.

Source	a, Å	b, Å	c, Å	V, Å^3	α, deg	β, deg	γ, deg	ρ, g.cm^{-3}
ClayFF-orig (This work)	11.162	11.165	21.623	2333.5	90.05	89.95	119.97	1.811
ClayFF-MOH (This work)	11.148	11.139	21.673	2330.7	89.97	89.98	119.97	1.814
ClayFF-orig [21]	11.02	10.94	21.30	2232.3	90.50	89.80	119.80	1.710
ClayFF-orig [32]	10.96	10.96	20.95	2179.4	90	90	120	1.91
DFT [32]	11.17	11.17	21.35	2306.9	90	90	120	1.81
DFT [18]	11.223	11.223	21.867	2385.4	90	90	120	1.747

DFT [24]	11.289	11.289	21.617	2385.6	90	90	120	1.747
AFFF[43]	11.284	11.284	21.506	2371.6	90	90	120	1.758
Neutron diffraction [48]	11.1668	11.167	21.354	2306.4	90	90	120	1.900
X-ray diffraction [49]	11.229	11.229	21.478	2345.5	90	90	120	1.772
X-ray diffraction [46]	11.26	11.26	21.48	2358.5	90	90	120	1.76

The equilibrium crystallographic unit cell parameters and density of ettringite, calculated with the ClayFF-orig and ClayFF-MOH force fields, are presented in Table 1. They are compared with available experimental data [46, 48-49] and earlier simulation results obtained by classical MD methods [21, 32] and DFT-calculations [18, 24, 32].

It is worth mentioning that, unlike most simulation results presented in Table 1, our simulations were performed in the *NPT* statistical ensemble without any symmetry constrains imposed on the system, and all crystal cell parameters were allowed to vary. Nevertheless, present results are in close agreement with the experimental and DFT-calculated values. No significant differences in the crystallographic parameters and densities between the ClayFF-orig and ClayFF-MOH models are also observed, indicating that taking into account the explicit M−O−H angle bending terms for structural hydroxides in ettringite has no effect on bulk density and crystallographic parameters.

3.2. Elastic properties of crystalline ettringite

The calculated at normal conditions elastic constants of ettringite in Voigt notation are presented in Table 2. All elastic constants were calculated independently without taking into account the symmetry constraints of the crystal. For the constants that should be identical or zero due to the crystal symmetry, the differences in the calculated results were below 6 GPa for the ClayFF-orig model and below 4 GPa for the ClayFF-MOH model. In comparison of

the calculated elastic constants with experimental data [58], the ClayFF-MOH force field gives a better agreement. Especially the value of C_{33} shows a significant improvement. This can be explained by a formation of a more structured intra-crystalline network of hydrogen bonds in ettringite when modeled with the ClayFF-MOH version of the force field due to the application of more realistic constraints on the amplitudes of Al-O-H and Ca-O-H angle bending librations. The value of the elastic constant C_{33} is still lower than the ones observed experimentally [57], in DFT calculations [19], or in reactive MD simulations [25, 38], but it is very comparable with the results of MD simulations using other classical force fields [43, 59].

In summary, the ClayFF-MOH version of the force field results in better predictions for the bulk modulus, shear modulus, Young modulus and the Poisson ratio due to the formation of a stronger and more structured network of hydrogen bonds between hydroxyls and water molecules in this model. The critical importance of the hydrogen bonding contribution to the elastic properties of ettringite has also been demonstrated recently in DFT calculations at high pressures [24].

Table 2. Elastic properties of ettringite under ambient conditions.

	This work		Exp. [57]	DFT [19]	ReaxFF MD [38]	ReaxFF MD [25]	Classical MD [43]	Classical MD [59]
	ClayFF -orig	ClayFF -MOH						
C_{11} (GPa)	33.0	31.0	35.1±0.1	39.5	45.4	30.0	36.6	36.5
C_{33} (GPa)	31.7	45.6	55.1±0.1	57.1	53.9	52.0	47.5	49.86
C_{12} (GPa)	16.4	18.5	21.9±0.1	25.7	25.0	20.1	19.0	18.5
C_{13} (GPa)	18.7	15.1	20.0±0.5	19.7	23.0	20.0	15.9	18.31
C_{44} (GPa)	5.3	5.9	11.0±0.2	10.0	11.1	12.2	9.3	12.06
C_{66} (GPa)	5.6	7.6	6.6±0.1	6.9	8.1	4.9	10.7	8.85
K (GPa)	29.8	26.1	27.3±0.9	29.4	26.76	25.8	24.7	25.57
G (GPa)	5.8	7.8	9.5±0.8	9.6	12.44	12.2	9.2	10.63
E (GPa)	16.4	21.4	25.0±2.0	26.0	-	-	24.5	28.0
ν	0.41	0.36	0.34±0.02	0.35	0.30	0.335	0.34	0.32

For the shear modulus (G) of ettringite, the ClayFF-MOH gives quite acceptable deviations from the experimental and theoretical results, but it also causes a somewhat lower value for the Young modulus, (E). This can be explained by the absence of explicit parametrization of covalent bonds in the ClayFF model due to its quasi-ionic character [39, 40]. However, as it was demonstrated earlier [24], the ionic-covalent bonds are predominant along the c axis of the crystal. This can also explain a not very accurate reproduction of the longitudinal elastic anisotropy ratio (C_{66}/C_{44}), compared to both experimental data [58] and DFT calculations [19]. However, the ratio C_{11}/C_{33} reflecting the general elastic anisotropy of ettringite is described much better with the ClayFF-MOH version of the force field (0.68), in very good agreement with experiment and DFT calculations (0.64 and 0.69, respectively).

3.3. Structure and dynamics of hydrogen bonding in crystalline ettringite

In ettringite crystal, there are two structurally distinct types of H_2O molecules: the ones belonging to ettringite columns and the ones located in the ettringite channels between SO_4^{2-}tetrahedra. We mark the type latter with a (*) symbol in the following discussion. As the simulation progresses, some exchange between the two types of H_2O molecules can occur. That is, in the process of simulations, the molecules initially located in the ettringite channels can become the molecules of the ettringite columns and vice versa. The possibility of such exchange was taken into account in the calculations of hydrogen bonding statistics by using a geometric determination of the H_2O molecule location: they were considered belonging to the ettringite columns only if they were completely located within a cylinder with a radius of 4.6 Å centered around a column. The position of the cylinder axis for each column was calculated based on the average positions of the aluminum atoms in the respective column.

The H_2O molecules outside any such cylinders were considered belonging to the ettringite channels.

Both types of these structural water molecules can form hydrogen bonds among themselves, and also donate H-bonds to the O-atoms of sulphate anions (Os) and O-atoms of the structural –O-H groups (Oh). At the same time, H-atoms of the structural hydroxyls are also serving as H-bond donors to various acceptor sites. Thus, a total of 11 different H-bonding donor-acceptor pairs can be formed in the ettringite crystal (Table 3).

Table 3. The average number of H-bonds per H_2O molecule/donor (n) and the average lifetime of H-bond (τ).

Donor-acceptor pair	n_{HB}		τ_{HB}, ps	
	ClayFF-orig	ClayFF-MOH	ClayFF-orig	ClayFF-MOH
Hw⋯Ow	0.59	0.58	0.35	0.38
Hw*⋯Ow*	0.30	0.26	0.43	0.36
Hw⋯Ow*	0.09	0.09	0.38	0.37
Hw*⋯Ow	0.75	0.70	0.36	0.38
Hw⋯Os	1.38	1.38	>10	>10
Hw*⋯Os	0.81	0.83	>10	>10
Hw⋯Oh	0.01	~0 (rare event)	0.23	0.01
Hw*⋯Oh	~0 (rare event)	~0 (rare event)	0.10	0.01
Hh⋯Ow	0.74	0.89	0.29	>10
Hh⋯Ow*	~0 (rare event)	~0 (rare event)	0.03	0.01
Hh⋯Os	~0 (rare event)	~0 (rare event)	0.06	0.01

First, we looked at the average number of H bonds formed between the H_2O molecules of both types (see Table 3). For Hw-Ow pairs the average numbers of H bonds virtually coincide for both versions of the ClayFF force field. In comparison with bulk liquid water [60], such a small number of H-bonds per molecule is due to the fact that the H_2O molecules in the ettringite columns are confined and have a predominant orientation allowing them to accept H-bonds from the structural hydroxyl groups (Hh-Ow). For Hw*···Ow* pairs, an even lower average number of H-bonds is observed simply because of the small number of H_2O molecules of this type in the ettringite channels. The continuous time correlation functions (Eq. 6) of these H-bonds are similar for both types of pairs and decay to zero within ~3 ps (see Fig. 2). The average H-bonding lifetimes (τ) are also similar for both types of pairs and both versions of the ClayFF force field (see Table 3). These values are about an order of magnitude lower than the corresponding values for bulk liquid water [60], indicating weaker less stable H-bonds of these types in ettringite and a faster dynamics of their formation and breaking.

For the pair Hw···Ow* the H-bonds are only very rarely formed and they are equally short lived as the ones discussed above. At the same time, there is a significant number of Hw*···Ow H-bonds formed, but they are also equally short lived as the other water-water H-bonds above.

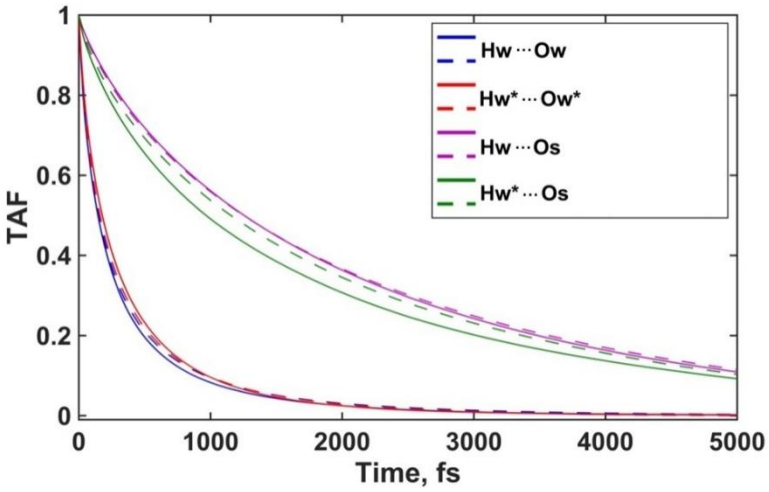

Figure 2. Continuous time autocorrelation functions (Eq. 6) of H-bonds donated by both types of H_2O molecules to other H_2O molecules and to SO_4^{2-} ions.Solid lines – ClayFF-orig; dashed lines – ClayFF-MOH

The largest average number of H-bonds and their longest average lifetimes are observed for the pairs Hw···Os and Hw*···Os, e.g. the ones accepted by sulphate ions in the crystal structure from both types of water molecules (see Table 1). This is in very good agreement with the results of DFT calculations [18]. These H-bonds are very long lived and their corresponding time correlation functions do not fully decay even after 5 ps (see Fig.2). These results are very similar for both versions of the ClayFF force field, and it is safe to say that these are the most important H-bonds providing the structural stability for the ettringite crystals.

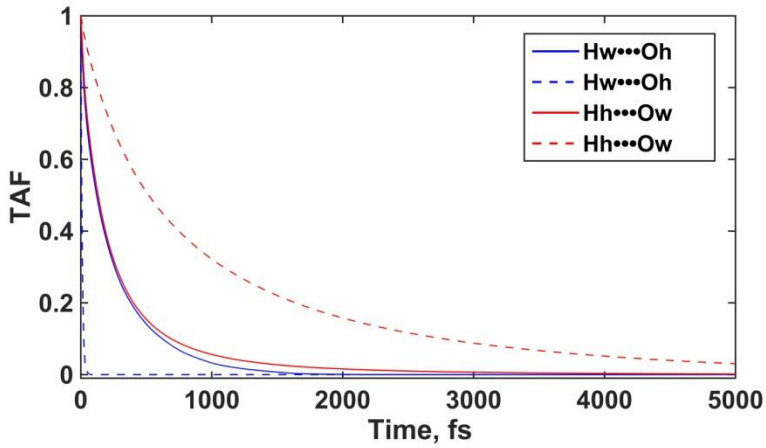

Figure 3. Continuous time autocorrelation functions (Eq. 6) of H-bonds accepted and donated by the structural hydroxyl groups to H_2O molecules belonging to the ettringite columns. Solid lines – ClayFF-orig; dashed lines – ClayFF-MOH

Oxygen atoms of the structural hydroxyl groups can only extremely rarely accept H-bonds from any H_2O molecule, and this is even more evident when the M-O-H angles are properly constrained within the ClayFF-MOH model (Table. 3).

However, the bonds donated by the hydroxyl groups to the H_2O molecules belonging to the columns of ettringite are quite significant (the average number of H-bonds per donor is close to 1 for both versions ClayFF). In addition, they become particularly long lived when the structural M-O-H angles are properly constrained within the new ClayFF-MOH model (see the last two columns of Table 3 and also the dashed lines in Fig.3). This additional strengthening of the H-bonding network within the ettringite crystal with the new more accurate ClayFF model clearly represents the molecular mechanism responsible for a better description of the elastic properties of ettringite, as discussed in the previous section.

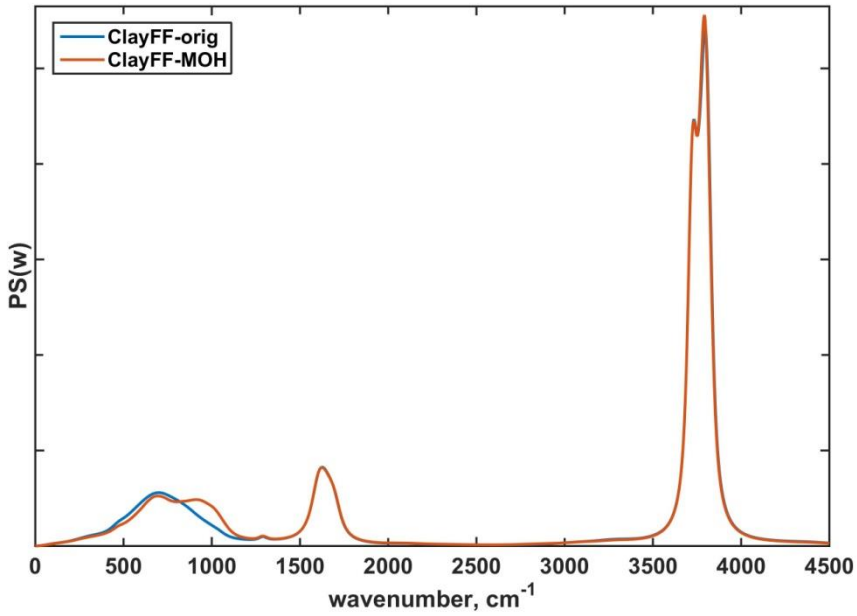

Figure 4. Total power spectra of the ettringite crystal models. Blue solid lines – ClayFF-orig; red solid lines – ClayFF-MOH.

Power spectra (Eq.3) of different modes of atomic vibrations in the crystal provide another useful way to assess the contribution of H-bonding to the properties of ettringite. Figure 4 shows the total power spectra (classical vibrational density of states) calculated for both versions of ClayFF. In terms of the major peak positions, they are in generally good agreement with available experimental IR spectra [18, 58, 61, 62] and the results of DFT calculations [18]. As expected, for both versions of ClayFF, the calculated spectra virtually coincide over the entire spectral range, except around the area of ~1000 cm^{-1} corresponding to the modes of M-O-H bending vibrations, where the effect of the new modification of the ClayFF force field is the most visible.

The peaks reflecting the O-H stretching modes of hydroxyls and H_2O molecules are located at ~3730 cm^{-1} and ~3790 cm^{-1}, which is slightly further than the experimental data and data of DFT calculations [18, 63]. This is expected due to the use of simple harmonic functions for the description of these intramolecular vibrations. A more elaborate potential for

H_2O intramolecular motions would be necessary to better reproduce the positions and widths of these peaks (e.g., [53]). However, the peak reflecting the H_2O angular bending mode (deformation) at ~1624 cm^{-1} is in excellent agreement with experimental data [63] and DFT calculations [18].

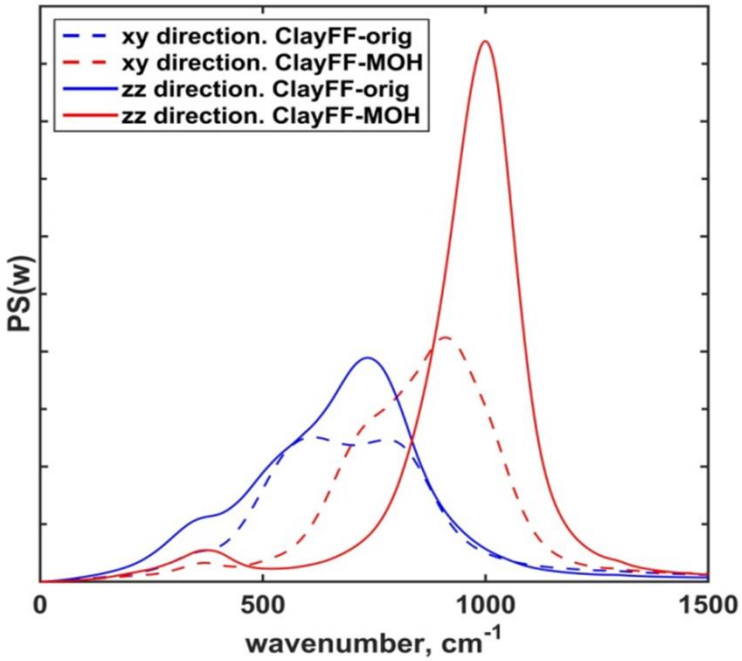

Figure 5. Power spectra of H-atoms belonging to the structural hydroxyl groups and their individual components along the crystal axis (*zz*) and perpendicular to the crystal axis (*xy*) of ettringite. Blue lines – ClayFF-orig; red lines – ClayFF-MOH.

Yet again, due to the use of a simple harmonic model to describe intramolecular bonds of the sulphate anions, there is a slight deviation from the experimental data [63] of the S-O bond stretching peak position which is located at ~1290 cm^{-1} for both versions of the ClayFF force field. In the calculated total spectra (Fig.4) and experimental Raman spectra [63] this spectral range overlaps with the M-O-H bending modes of the structural hydroxyls – the primary focus of our study. However, Figure 5 provides a much more detailed view of this spectral range, calculated through the VACFs of H-atoms of structural hydroxyls, thus

excluding the contributions from the sulphate vibrations. The calculated spectra in Fig. 5 are additionally separated into two distinct contributions of the vibrational motions of structural hydroxyls: parallel to the crystal axis (*z*) and within the plane perpendicular to it (*xy*). For the ClayFF-MOH model, the sharper peaks shifted to higher frequencies clearly reflect the more restrained M-O-H bending vibrations.

3.4. Structure of ettringite-solution interfaces

The density profiles of hydrogen and oxygen atoms of all types of water molecules (Hw, Ow) in the system with Na_2SO_4 aqueous solution are shown in Fig.6. For a system containing NaCl aqueous solution, the Hw and Ow atomic density profiles look very similar.

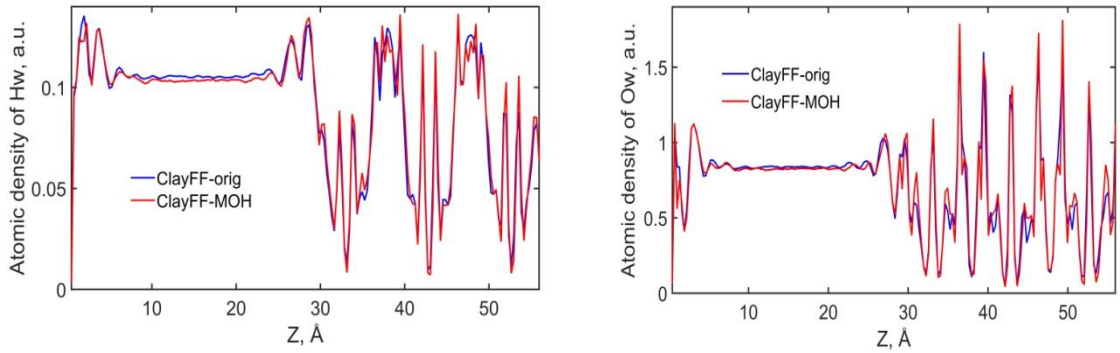

Figure 6. Atomic density profiles of Hw (left) and Ow (right) for the system with Na_2SO_4 solution. Aqueous solution located from ~1 Å to ~30 Å along the *z* axis.

Our results are consistent with the earlier calculated density profiles of these atoms [35]. However, the primary difference between the ClayFF-MOH and ClayFF-orig models is that for the modified force field the peaks of both Hw and Ow distributions are somewhat sharper in the locations where the interfacial and intercolumnar H_2O molecules directly interact with structural O-H groups. This is clearly caused by a more accurately defined

orientation of these O-H groups, constrained by the new M−O−H angle bending term, leading to a more localized positioning of the H_2O molecules forming stronger donating and, especially, accepting H-bonds with these O-H groups, compared with the ClayFF-orig unconstrained model.

Atomic density profiles of Na^+ and Cl^- ions in aqueous solution at the ettringite surface are shown in Figure 7. Integration of the density profiles shows that the density of Na^+ ions in solution near the surface of ettringite decreases by ~30% and the density of Cl^- increases by ~20% with the new modified ClayFF-MOH force field. This, of course, reflects significant changes in the ionic adsorption patterns. In particular, the closest to the ettringite surface peak of the Na^+ distribution in the ClayFF-orig force field (~0 Å from the surface) is completely missing in the results of the ClayFF-MOH force field.

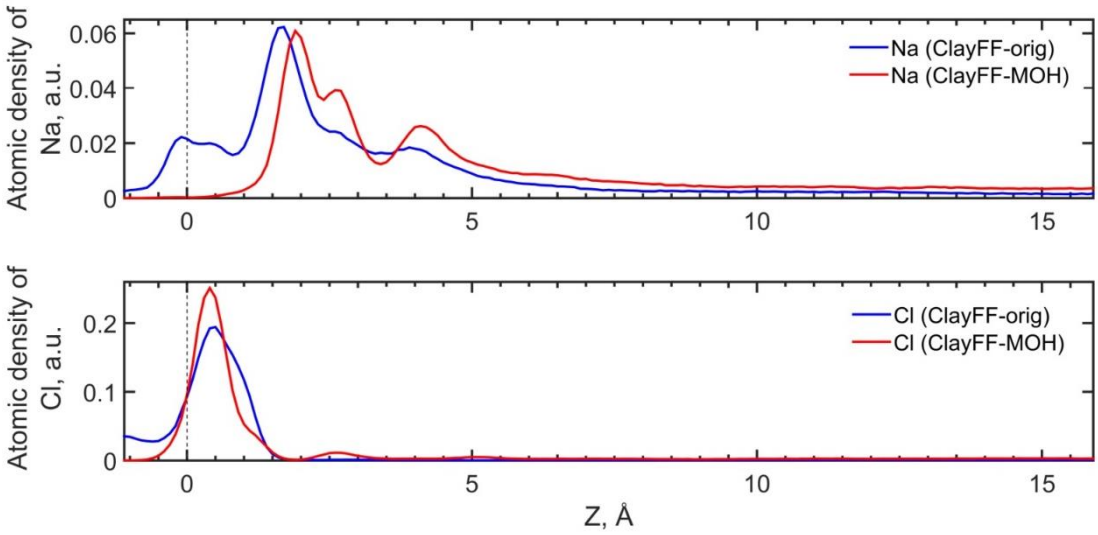

Figure 7. Atomic density profiles of Na^+ (top) and Cl^- (bottom) ions in aqueous solution at the surface of ettringite. The first 3.5Å-thicklayer of solution (*a*) is right next to the surface. The second 3.5Å-thicklayer of solution (*b*) is farther away from the surface. Beyond layer (*b*) we consider the solution to be in nearly the bulk phase (*c*). (See Fig.1 for a detailed illustration).

The first peak of Na^+ adsorption in the ClayFF-MOH simulation is a combination of the high subpeak located ~1.9 Å from the surface and a low subpeak ~2.6 Å from the surface. The results for the ClayFF-orig simulation also show two poorly resolved adsorption peaks at those distances, but with the high peak being further from the surface. Both force fields result in a peak of Na^+ density around ~3.4 Å from the ettringite surface, with the slightly lower magnitude for the ClayFF-MOH version. These changes in the location of the peaks and their magnitude indicate that the inner-sphere coordination of Na^+ ions changes in the first layer (*a*) of solution for the ClayFF-MOH force field.

On the other hand, the Cl^- profile for the first layer of solution (*a*) for the ClayFF-MOH simulation does not change qualitatively, but for the ClayFF-MOH the first peak is sharper and somewhat closer to the surface, indicating a stronger inner-sphere adsorption of Cl^- in this case. A larger amount of outer-sphere adsorption at ~2.5 Å is also visible in the ClayFF-MOH simulation.

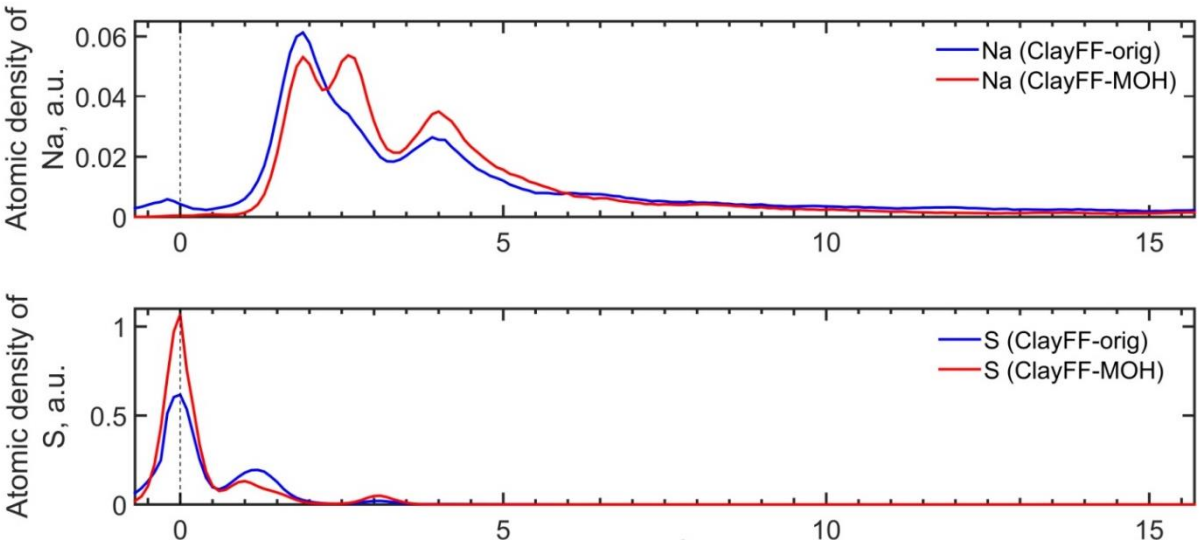

Figure 8. Atomic density profiles of Na^+ (top) and SO_4^{2-} ions (bottom) ions in aqueous solution at the surface of ettringite. Only the distribution of S-atoms of sulphate is shown.

Figure 8 shows the atomic density profiles of Na^+ and SO_4^{2-} ions for the simulated interface of ettringite with Na_2SO_4 aqueous solution. For the modified ClayFF-MOH force field, the distribution of Na^+ ions is very similar to the one observed for the system with NaCl aqueous solution. However, significant differences are observed in the near-surface distribution of SO_4^{2-} ions between the two versions of the force field. It is worth to remember that for this system the SO_4^{2-} ions initially belonging to the ettringite structure and the ones initially present in solution are indistinguishable, and some dissolution/exchange is possible. Therefore, the sharper and higher first peaks of S in Fig. 8 (inner-sphere surface coordination) and lower second peaks (outer-sphere surface coordination) for the ClayFF-MOH model clearly indicate that in this case the structural SO_4^{2-} ions are more strongly held in place by H-bonding to surface hydroxyls, and the ionic dissolution/exchange occurs to a much lesser extent.

The atomic density distributions on the surface in the form of contour maps provide an additional dimension to our understanding of the mineral-solution interfaces. Figure 9 shows such contour maps for the first solution layer (*a*) on the ettringite surface with NaCl solution (top) and Na_2SO_4 solution (bottom) calculated with the ClayFF-orig (left) and ClayFF-MOH (right) versions of the force field. On the maps for the ClayFF-MOH version, a much stronger localization of atomic density is observed for all solution species (Ow, Na, Cl, S, Os), which is clearly the result of more accurate constraints imposed on the M-O-H angle bending on the crystal surface. This also indirectly indicates that diffusional mobility of species might be decreasing on the surface with this model.

In both solutions and for both versions of the force field, the surface location of adsorbed Na^+ ions is always coordinated with the interfacial SO_4^{2-} ions, due to strong electrostatic attraction between them. However, it is noticeable that the ettringite sulphates

can be displaced into solution at some surface sites by Cl^- ions for the NaCl solution interface. In contrast, the surface density of sulphates for the Na_2SO_4 solution interface seems to increase. This is consistent with the calculated interfacial atomic density profiles, as discussed above.

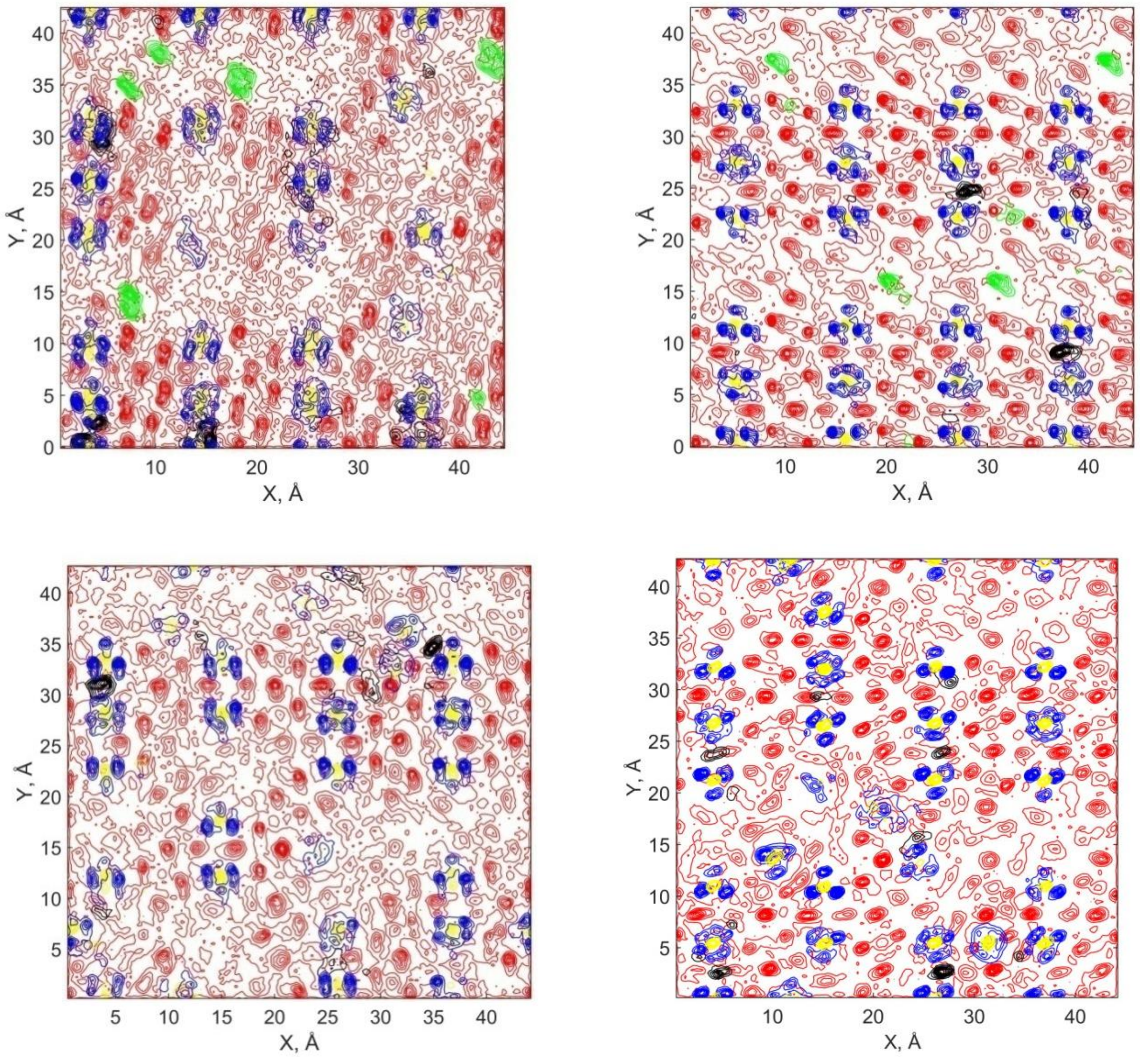

Figure 9. Time-averaged atomic density distributions of aqueous species in the first solution layer (*a*) on the surface of ettringite. Top panels – NaCl solution, bottom panels – Na_2SO_4 solution. Left column – ClayFF-orig; right column – ClayFF-MOH. Red countours – Ow; black contours – Na^+; green contours – Cl^-; yellow contours – S of sulphate, blue contours – Os of sulphate.

However, it is also noticeable that the surface structure of the ettringite crystal is more disturbed at the interface with Na_2SO_4 solution than with NaCl. Such partial destruction of the surface ordering in the positions of the sulphate ions, even more pronounced for the more accurate ClayFF-MOH model, seems to be consistent with the view that sulphate-containing waters are primarily responsible for such corrosive damage to concrete and stimulate the production of more volumes of ettringite through the dissolution/precipitation processes.

3.5. Diffusional mobility of water and ions in ettringite nanopores

Due to the relatively small number of solution ions in all simulated systems, only bulk 3-dimensional diffusion coefficients were calculated for them, taking into account the entire aqueous nanopore (Eq. 10). The average self-diffusion coefficients for the ions are found to be $D_{Na} = (1.5\pm0.2)\times10^{-6}$ cm^2/s, $D_{Cl} = (2.1\pm0.2)\times10^{-6}$ cm^2/s, $D_S = (5.5\pm0.5)\times10^{-7}$ cm^2/s, with only marginal differences between both versions of the force field. These values are in good agreement with the results of earlier calculations with the ClayFF-orig version of the force field [21, 35].

However, for H_2O molecules in solution, more detailed calculations of 2-dimensional diffusion coefficients were performed separately for the (*a*), (*b*), and (*c*) solution layers (see Fig.1). As expected, they have shown that the diffusional mobility of water molecules decreases as they approach the surface, with $D_{H2O}{}^{c} = (2.7\pm0.2)\times10^{-5}$ cm^2/s, $D_{H2O}{}^{b} = (2.0\pm0.2)\times10^{-5}$ cm^2/s, and $D_{H2O}{}^{a} = (1.2\pm0.2)\times10^{-5}$ cm/s. Compared to the original ClayFF parametrization, ClayFF-MOH has resulted in ~10% lower diffusion coefficients in all layers of the NaCl solution, but in ~10% higher diffusion coefficients in all layers of the Na_2SO_4. These differences seem systematic, but they are definitely within the statistical uncertainty of the present calculations.

4. CONCLUSIONS

ClayFF force field is currently widely used for atomistic simulations of various cementitious systems [16, 40]. A new version of this force field, ClayFF-MOH has been recently developed to more accurately model the hydrated edges of various hydroxides, clays, and similar materials [40, 44, 45]. The extra interaction terms introduced in that version more accurately constrain any Metal-O-H bending angles ubiquitous in many cementitious materials as well. Here we tested the applicability of this new parametrization by detailed quantitative comparison of molecular simulation results for a bulk crystal of ettringite and its interfaces with aqueous solutions of NaCl and Na_2SO_4 with available experimental data and results produced by the original version of ClayFF earlier and in the course of this study.

Ettringite, $Ca_6[Al(OH)_6]_2[SO_4]_3 \cdot 26H_2O$, contains two such relevant bending terms in its structure: Al−O−H and Ca−O−H. The results of our comparison show that explicit inclusion of these angular bending terms into the force field does not affect the reproduction of the crystallographic unit cell parameters of ettringite and, at the same time, noticeably improves the reproduction of elastic properties of the bulk crystal and its vibrational properties. All these effects can be consistently explained by the formation of a stronger and more stable hydrogen bonding network in the intercolumnar space of ettringite crystals and at their surfaces. This leads to a stronger immobilization of the H_2O molecules within the structure, as well as on the surface. The new model also seem to demonstrate slightly stronger ionic adsorption at the ettringite surface than it was earlier predicted by the original ClayFF model.

5. ACKNOWLEDGMENTS

The article was prepared within the framework of the HSE University Basic Research Program. This research was supported in part through computational resources of HPC facilities at HSE University [64]. A.G.K. also acknowledges the financial support of the industrial chair “Storage and Disposal of Radioactive Waste” at the IMT-Atlantique, funded by ANDRA, Orano, and EDF.

REFERENCES

[1] K.L. Scrivener, R.J. Kirkpatrick, Innovation in use and research on cementitious material, Cement and Concrete Research 38 (2008) 128-136, https://doi.org/10.1016/j.cemconres.2007.09.025

[2] M. A. Sanjuán, A. Zaragoza, J. C. L. Agüí, Standardization for an innovative world, Cement and Concrete Research 41 (2011) 767-774, https://doi.org/10.1016/j.cemconres.2011.03.015

[3] H. Van Damme, Concrete material science: Past, present, and future innovations, Cement and Concrete Research 112 (2018) 5-24, https://doi.org/10.1016/j.cemconres.2018.05.002

[4] R. Snellings, G. Mertens, J. Elsen, Supplementary cementitious materials, Reviews in Mineralogy and Geochemistry 74 (2012) 211-278, https://doi.org/10.2138/rmg.2012.74.6

[5] M.C.G. Juenger, R. Siddique, Recent advances in understanding the role of supplementary cementitious materials in concrete, Cement and Concrete Research 78 (2015) 71-80, https://doi.org/10.1016/j.cemconres.2015.03.018

[6] M. Collepardi, A state-of-the-art review on delayed ettringite attack on concrete, Cem. Concr. Composites 25 (2003) 401-407, https://doi.org/10.1016/S0958-9465(02)00080-X

[7] P.M. Carmona-Quiroga, M.T. Blanco-Varela, Ettringite decomposition in the presence of barium carbonate, Cement and Concrete Research 52 (2013) 140-148, https://doi.org/10.1016/j.cemconres.2013.05.021

[8] W. Müllauer, R. E. Beddoe, D. Heinz, Sulfate attack expansion mechanisms, Cement and Concrete Research 52 (2013) 208-215, https://doi.org/10.1016/j.cemconres.2013.07.005

[9] H.F.W. Taylor, C. Famy, K.L. Scrivener, Delayed ettringite formation, Cement and Concrete Research 31 (2001) 683-693, https://doi.org/10.1016/S0008-8846(01)00466-5

[10] H.F.W. Taylor, 1997. Cement Chemistry, second ed., Thomas Telford Publishing, 480p.

[11] J. Lehmann, Uber den Ettringit, ein neues Mineral in Kalkeinschlussen der Lava von Ettringen (Laacher Gebiet), Neues Jahrbuch Mineralogie, Geologie und Palaontologie, 1874, 273-275.

[12] A. Martucci, G. Cruciani, In situ time resolved synchrotron powder diffraction study of thaumasite, Physics and Chemistry of Minerals 33 (2006) 723-731, https://doi.org/10.1007/s00269-006-0124-8

[13] A.G. Kalinichev, J.W. Wang, R.J. Kirkpatrick, Molecular dynamics modeling of the structure, dynamics and energetics of mineral-water interfaces: Application to cement materials, Cement and Concrete Research 37 (2007) 337-347, https://doi.org/10.1016/j.cemconres.2006.07.004

[14] F. Sanchez, K. Sobolev, Nanotechnology in concrete - A review, Construction and Building Materials 24 (2010) 2060-2071, https://doi.org/10.1016/j.conbuildmat.2010.03.014

[15] J.J. Biernacki, J.W. Bullard, G. Sant, K. Brown, F.P. Glasser, S. Jones, T. Ley, R. Livingston, L. Nicoleau, J. Olek, F. Sanchez, R. Shahsavari, P.E. Stutzman, K. Sobolev, T. Prater, Cements in the 21st century: Challenges, perspectives, and opportunities,

Journal of the American Ceramic Society 100 (2017) 2746-2773, http://dx.doi.org/10.1111/jace.14948

[16] R. K. Mishra, A. K. Mohamed, D. Geissbühler, H. Manzano, T. Jamil, R. Shahsavari, A. G. Kalinichev, S. Galmarini, L. Tao, H. Heinz, R. Pellenq, A. C.T. van Duin, S. C. Parker, R. J. Flatt, P. Bowen, CemFF: A force field database for cementitious materials including validations, applications and opportunities, Cement and Concrete Research, 102 (2017) 68-89, https://doi.org/10.1016/j.cemconres.2017.09.003

[17] R. J.-M. Pellenq, A. Kushima, R. Shahsavari, K. J. Van Vliet, M. J. Buehler, S. Yip, F.-J.Ulm A realistic molecular model of cement hydrates, Proceedings of the National Academy of Sciences 106 (2009) 16102-16107, https://doi.org/10.1073/pnas.0902180106

[18] E. Scholtzova, L. Kuckova, J. Kozisek, D. Tunega, Structural and spectroscopic characterization of ettringite mineral - combined DFT and experimental study, Journal of Molecular Structure 1100 (2015) 215-224, https://doi.org/10.1016/j.molstruc.2015.06.075

[19] E. Scholtzova, D. Tunega, S. Speziale, Mechanical properties of ettringite and thaumasite -DFT and experimental study, Cement and Concrete Research 77 (2015) 9-15, https://doi.org/10.1016/j.cemconres.2015.06.008

[20] J. Claverie, S. Kamali-Bernard, J.M.M. Cordeiro, F. Bernard, Assessment of mechanical, thermal properties and crystal shapes of monoclinic tricalcium silicate from atomistic simulations, Cement and Concrete Research 140 (2021), 106269, https://doi.org/10.1016/j.cemconres.2020.106269

[21] A.G. Kalinichev, R.J. Kirkpatrick, Molecular dynamics modeling of chloride binding to the surfaces of calcium hydroxide, hydrated calcium aluminate, and calcium silicate phases, Chemistry of Materials 14 (2002) 3539-3549, https://doi.org/10.1021/cm0107070

[22] M. Medala, C. Labbez, I. Pochard, A. Nonat, Ettringite surface chemistry: Interplay of electrostatic and ion specificity. Journal of Colloid and Interface Science 354 (2011) 765-770, https://doi.org/10.1016/j.jcis.2010.11.031

[23] H. Manzano, R.J.M. Pellenq, F.-J. Ulm, M.J. Buehler, A.C.T. van Duin, Hydration of calcium oxide surface predicted by reactive force field molecular dynamics, Langmuir 28 (2012) 4187-4197, http://dx.doi.org/10.1021/la204338m

[24] H. Manzano, A. Ayuela, A. Telesca, P. J. M. Monteiro, J. S. Dolado, Ettringite strengthening at high pressures induced by the densification of the hydrogen bond network, Journal of Physical Chemistry C 116 (2012) 16138-16143, https://doi.org/10.1021/jp301822e

[25] W. Sun, D. Wang, L. Wang, Molecular dynamic simulation of failure of ettringite, Journal of Physics: Conference Series 419 (2013) 012011. https://doi.org/10.1088/1742-6596/419/1/012

[26] R. K. Mishra, L. Fernández-Carrasco, R. J. Flatt, H. Heinz, A force field for tricalcium aluminate to characterize surface properties, initial hydration, and organically modified interfaces in atomic resolution, Dalton Transactions, 43 (2014) 10602-10616, http://dx.doi.org/10.1039/C4DT00438H

[27] Q. Wang, H. Manzano, Y. Guo, I. Lopez-Arbeloa, X. Shen, Hydration mechanism of reactive and passive dicalcium silicate polymorphs from molecular simulations, Journal of Physical Chemistry C 119 (2015) 19869-19875, https://doi.org/10.1021/acs.jpcc.5b05257

[28] S. Galmarini, P. Bowen, Atomistic simulation of the adsorption of calcium and hydroxyl ions onto portlandite surfaces - towards crystal growth mechanisms, Cement and Concrete Research 81 (2016) 16-23, https://doi.org/10.1016/j.cemconres.2015.11.008

[29] E. Pustovgar, R.K. Mishra, M. Palacios, J.-B. d'Espinose de Lacaillerie, T. Matschei, A.S. Andreev, H. Heinz, R. Verel, R.J. Flatt, Influence of aluminates on the hydration kinetics of tricalcium silicate, Cement and Concrete Research 100 (2017) 245-262, https://doi.org/10.1016/j.cemconres.2017.06.006

[30] I. Androniuk, C. Landesman, P.Henocq, A.G. Kalinichev, Adsorption of gluconate and uranyl on C-S-H phases: Combination of wet chemistry experiments and molecular dynamics simulations for the binary systems, Physics and Chemistry of the Earth 99 (2017) 194-203, https://doi.org/10.1016/j.pce.2017.05.005

[31] I. Androniuk, A.G. Kalinichev, Molecular dynamics simulation of the interaction of uranium (VI) with the C-S-H phase of cement in the presence of gluconate, Applied Geochemistry 113 (2020) 104496, https://doi.org/10.1016/j.apgeochem.2019.104496 .

[32] S. M. Mutisya,J. M. de Almeida, C. R.Miranda, Molecular simulations of cement based materials: A comparison between first principles and classical force field calculations, Computational Materials Science 138 (2017) 392-402, https://doi.org/10.1016/j.commatsci.2017.07.009

[33] Q. Ding, J. Yang, D. Hou, G. Zhang, Insight on the mechanism of sulfate attacking on the cement paste with granulated blast furnace slag: An experimental and molecular dynamics study, Construction and Building Materials 169 (2018) 601-611, https://doi.org/10.1016/j.conbuildmat.2018.02.148

[34] A. Kremleva, S. Kruger, N. Rosch, Uranyl(VI) sorption in calcium silicate hydrate phases. A quantum chemical study of tobermorite models, Applied Geochemistry 113 (2020) : 104463, https://doi.org/10.1016/j.apgeochem.2019.104463

[35] S. Hajilar, B. Shafei, Atomic-scale investigation of physical adsorption of water molecules and aggressive ions to ettringite's surfaces. Journal of Colloid and Interface Science, 513 (2018) 104-116, https://doi.org/10.1016/j.jcis.2017.09.019

[36] R. Shahsavari, R.J.M. Pellenq, F.-J. Ulm, Empirical force fields for complex hydrated calcio-silicate layered materials, Phys. Chem. Chem. Phys. 13 (2011) 1002-1011, http://dx.doi.org/10.1039/C0CP00516A

[37] H. Heinz, T. J. Lin, R. K. Mishra, F. S. Emami, Thermodynamically consistent force fields for the assembly of inorganic, organic, and biological nanostructures: The INTERFACE force field, Langmuir 29 (2013) 1754-1765, http://dx.doi.org/10.1021/la3038846

[38] L. Liu, A. Jaramillo-Botero, W. A. Goddard, H. Sun, Development of a ReaxFF reactive force field for ettringite and study of its mechanical failure modes from reactive dynamics simulations, Journal of Physical Chemistry A 116 (2012) 3918-3925, https://doi.org/10.1021/jp210135j

[39] R.T. Cygan,, J.-J. Liang, A. G. Kalinichev, Molecular models of hydroxide, oxyhydroxide, and clay phases and the development of a general force field, Journal of Physical Chemistry B 108 (2004) 1255-1266, https://doi.org/10.1021/jp0363287

[40] R.T. Cygan, J.A. Greathouse, A.G.Kalinichev, Advances in Clayff molecular simulation of layered and nanoporous materials and their aqueous interfaces. Journal of Physical Chemistry C 125 (2021) 17573-17589, https://doi.org/10.1021/acs.jpcc.1c04600

[41] R.T.Cygan, J.A.Greathouse, H.Heinz, A.G.Kalinichev, Molecular models and simulations of layered materials. Journal of Materials Chemistry 19 (2009) 2470-2481, http://dx.doi.org/10.1039/b819076c

[42] B. F. Ngouana-Wakou, A. G. Kalinichev, Structural arrangements of isomorphic substitutions in smectites: Molecular simulation of the swelling properties, interlayer structure, and dynamics of hydrated Cs-montmorillonite revisited with new clay models, Journal of Physical Chemistry C 118 (2014) 12758-12773, http://dx.doi.org/10.1021/jp500538z

[43] T. Honorio, P. Guerra, A. Bourdot, Molecular simulation of the structure and elastic properties of ettringite and monosulfoaluminate, Cement and Concrete Research 135 (2020) 106126, https://doi.org/10.1016/j.cemconres.2020.106126

[44] M. Pouvreau, J. A. Greathouse, R. T. Cygan, A. G. Kalinichev, Structure of hydrated gibbsite and brucite edge surfaces: DFT results and further development of the ClayFF classical force field with Metal-O-H angle bending terms, Journal of Physical Chemistry C 121 (2017) 14757-14771, http://dx.doi.org/10.1021/acs.jpcc.7b05362

[45] M. Pouvreau, J. A. Greathouse, R. T. Cygan, A. G. Kalinichev, Structure of hydrated kaolinite edge surfaces: DFT results and further development of the ClayFF classical force field with Metal-O-H angle bending terms, Journal of Physical Chemistry C (123) 2019 11628-11638, https://doi.org/10.1021/acs.jpcc.9b00514

[46] A. Moore, H. F. W. Taylor, Crystal structure of ettringite, Nature 218 (1968) 1048-1049, https://doi.org/10.1038/2181048a0

[47] A. Moore, H. F. W. Taylor, Crystal structure of ettringite, Acta Crystallographica B 26 (1970) 386-393, https://doi.org/10.1107/S0567740870002443

[48] M.R. Hartman, R. Berliner. Investigation of the structure of ettringite by time-of-flight neutron powder diffraction techniques, Cement and Concrete Research 36(2006)364-370, https://doi.org/10.1016/j.cemconres.2005.08.004

[49] F. Goetz-Neunhoeffer, J. Neubauer. Refined ettringite $Ca_6Al_2(SO_4)_3(OH)_{12}\cdot 26H_2O$ structure for quantitative X-ray diffraction analysis, Powder Diffraction 21 (2006) 4-11, https://doi.org/10.1154/1.2146207

[50] A.M. Cody, H. Lee, R.D. Cody, P.G. Spry, The effects of chemical environment on the nucleation, growth, and stability of ettringite $[Ca_3Al(OH)_6]_2(SO_4)_3\cdot 26H_2O$, Cement and Concrete Research 34 (2004) 869-881, https://doi.org/10.1016/j.cemconres.2003.10.023

[51] S. Plimpton, Fast parallel algorithms for short-range molecular dynamics, Journal of Computational Physics 117 (1995) 1-19, https://doi.org/10.1006/jcph.1995.1039

[52] M.P. Allen, D.J. Tildesley, Computer Simulation of Liquids. 2nd Edition, Oxford University Press, New York, 2017, 626pp.

[53] M.Szczerba, A.Kuligiewicz, A.Derkowski, V.Gionis, G.D.Chryssikos, A.G.Kalinichev, Structure and dynamics of water-smectite interfaces: hydrogen bonding and the origin of the sharp O-D_W/O-H_W infrared band from molecular simulations. Clays and Clay Minerals 64 (2016), 452-471, https://doi.org/10.1346/ccmn.2016.0640409

[54] A.G.Kalinichev, P.P.Kumar, R.J.Kirkpatrick, Molecular dynamics computer simulations of the effects of hydrogen bonding on the properties of layered double hydroxides intercalated with organic acids, Philosophical Magazine 90 (2010), 2475-2488, https://doi.org/10.1080/14786430903559482

[55] N.Loganathan, A.G.Kalinichev, On the hydrogen bonding structure at the aqueous interface of ammonium-substituted mica: A molecular dynamics simulation. Zeitschrift für Naturforschung A 68 (2013), 91-100, https://doi.org/10.5560/zna.2012-0101

[56] A. Luzar, Resolving the hydrogen bond dynamics conundrum. Journal of Chemical Physics 113 (2000) 10663-10675, https://doi.org/10.1063/1.1320826

[57] J. Chanda, S. Bandyopadhyay, Hydrogen bond lifetime dynamics at the interface of a surfactant monolayer, Journal of Physical Chemistry B 110 (2006) 23443-23449, https://doi.org/10.1021/jp065203+

[58] S. Speziale, F. Jiang, Z. Mao, P.J.M. Monteiro, H.-R. Wenk, T.S. Duffy, F.R. Schilling, Single-crystal elastic constants of natural ettringite, Cement and Concrete Research 38 (2008) 885-889. https://doi.org/10.1016/j.cemconres.2008.02.004

[59] P. K. Sarkar, N. Mitra, D. Prasad, Molecular level deformation mechanism of ettringite. Cement and Concrete Research 124 (2019) 105836, https://doi.org/10.1016/j.cemconres.2019.105836

[60] S. Chowdhuri, A. Chandra, Hydrogen bonds in aqueous electrolyte solutions: Statistics and dynamics based on both geometric and energetic criteria, Phys. Rev. E, 66(2002) 041203, https://doi.org/10.1103/PhysRevE.66.041203

[61] S.M. Clark, B. Colas, M. Kunz, S. Speziale, P. J. M. Monteiro, Effect of pressure on the crystal structure of ettringite, Cement and Concrete Research 38 (2008) 19-26, https://doi.org/10.1016/j.cemconres.2007.08.029

[62] G.D. Gatta, U. Hålenius, F. Bosi, L. Cañadillas-Delgado, M.T. Fernandez-Diaz, Minerals in cement chemistry: A single-crystal neutron diffraction study of ettringite, $Ca_6Al_2(SO_4)_3(OH)_{12}\cdot 27H_2O$, American Mineralogist 104 (2019) 73-78, https://doi.org/10.2138/am-2019-6783

[63] R.L. Frost, A. López, Y. Xi, R. Scholz, G.M. da Costa, R.M.F. Lima, A. Granja, The spectroscopic characterization of the sulphate mineral ettringite from Kuruman manganese deposits, South Africa, Vibrational Spectroscopy 68 (2013) 266-271, https://doi.org/10.1016/j.vibspec.2013.08.011

[64] P.S. Kostenetskiy, R.A.Chulkevich, V.I. Kozyrev, HPC Resources of the Higher School of Economics, Journal of Physics: Conference Series, 1740 (2021), 012050, https://doi.org/10.1088/1742-6596/1740/1/012050